

See discussions, stats, and author profiles for this publication at: <https://www.researchgate.net/publication/271882742>

Multiobjective crashworthiness optimization of functionally lateral graded foam-filled tubes

Article in *Materials & Design* (1980-2015) · February 2013

DOI: 10.1016/j.matdes.2012.08.033

CITATIONS

106

READS

380

4 authors, including:



Hanfeng Yin

Hunan University

59 PUBLICATIONS 2,036 CITATIONS

SEE PROFILE



Guilin Wen

Hunan University

183 PUBLICATIONS 4,458 CITATIONS

SEE PROFILE



Shujuan Hou

Hunan University

70 PUBLICATIONS 3,588 CITATIONS

SEE PROFILE



Multiobjective crashworthiness optimization of functionally lateral graded foam-filled tubes

Hanfeng Yin^{a,b}, Guilin Wen^{a,b,*}, Shujuan Hou^{a,b}, Qixiang Qing^b

^a State Key Laboratory of Advanced Design and Manufacturing for Vehicle Body, Hunan University, Changsha, Hunan 410082, PR China

^b College of Mechanical and Vehicle Engineering, Hunan University, Changsha, Hunan 410082, PR China

ARTICLE INFO

Article history:

Received 31 May 2012

Accepted 13 August 2012

Available online 31 August 2012

Keywords:

Foam-filled tubes

Functionally graded foam

Crashworthiness

Multiobjective optimization

Finite element method

ABSTRACT

Foam-filled tubes have recently gained attention due to their excellent energy absorption capacity. In order to improve the crashworthiness of foam-filled tubes, the energy absorption characteristics of two kinds of functionally lateral graded foam-filled tubes (FLGFTs) are investigated in this paper. Based on the numerical results, it is found that each of the two kinds of FLGFTs has more excellent energy absorption capacity than the ordinary uniform foam-filled tube (UFT) with the same weight. In addition, it can also be found that the gradient exponential parameter m which controls the variation of foam density gives rise to significant effects on the crashworthiness of FLGFTs. Thus, in order to seek for the optimal gradient exponential parameter, the two kinds of FLGFTs are optimized by multiobjective particle swarm optimization (MOPSO) algorithm, aiming to achieve the maximum specific energy absorption (SEA) and the minimum peak crushing force (PCF). During the process of multiobjective optimization design, the 7th-order polynomial functions of SEA and PCF are established and found to be accurate enough for engineering design. The results obtained by optimizations further indicate that the optimal FLGFT performs more excellent energy absorption characteristics than ordinary UFT. The optimization design data is a good guidance for the crashworthiness design of FLGFTs.

© 2012 Elsevier Ltd. All rights reserved.

1. Introduction

Foam-filled thin-walled structures have extensive application prospect in automotive, aerospace, military equipment and other industries, due to their excellent energy absorption capacity and extraordinary light weight [1]. Foam-filled thin-walled structures can absorb more impacting energy than the corresponding non-filled thin-walled structures without increasing too much total weight [2]. Thus, many researchers had done a lot of work on studying the energy absorption characteristics of foam-filled thin-walled structures by using experimental, analytical and numerical methods during the past decades. The examples of recent research work on foam-filled thin-walled structures are listed in Table 1. From their investigations, it can be found that the filled foam can improve the crush strength not only because of its own strength but also through an interaction between the foam and the tube wall. In addition, it can be found that the energy absorption capacity of foam-filled thin-walled structures is mainly determined by the parameters of thin wall geometry and foam density when the

loading condition is fixed. The crashworthiness of foam-filled thin-walled structures with various thin wall geometry and foam density will be very different.

Based on the above, it is very necessary to optimize the crashworthiness of foam-filled thin-walled structures by seeking for the optimal thin wall geometry sizes and foam density. Zarei and Kröger [20,21] implemented the multicriteria design optimization (MDO) procedure to maximum the energy absorption and minimum the weight of foam-filled aluminum tubes. Hou et al. [22,23] developed a multiobjective optimization framework for optimizing thin-walled column filled with aluminum foam. In their optimization process, surrogate model techniques were used in order to reduce the computation cost. Bi et al. [24] optimized single and triple-cell hexagonal columns filled with aluminum foams aiming at maximum specific energy absorption (SEA) with the constraint of mean crushing force (MCF). Zhang et al. [25] optimized the crashworthiness of foam-filled bitubal square column using the Kriging meta-modeling technique as well as the genetic algorithm (GA) and non-dominated sorting genetic algorithm II (NSGA II).

The abovementioned analysis and optimization work mainly focuses on the uniform foam-filled thin-walled structures. In order to improve the crashworthiness of foam-filled thin-walled structures, the functionally graded foam (FGF) material [26–29] was recently considered to replace the uniform foam (UF) material. Sun et al.

* Corresponding author at: State Key Laboratory of Advanced Design and Manufacturing for Vehicle Body, Hunan University, Changsha, Hunan 410082, PR China. Tel.: +86 731 88821482; fax: +86 731 88822051.

E-mail address: glwen@hnu.edu.cn (G. Wen).

Table 1
Recent studies on foam-filled thin-walled structures.^a

Year	Researchers	Investigation objects	Loading conditions
<i>Mainly by experimental method</i>			
1986	Reid et al. [3,4]	Polyurethane foam-filled thin-walled square, rectangular, circular and tapered tubes	QS and D
1988	Reddy and Wall [5]	Polyurethane foam-filled thin-walled circular metal tubes	QS and D
2000	Santosa et al. [6]	Aluminum foam-filled square tubes	QS
2000	Hanssen et al. [7,8]	Aluminum foam-filled circular and square AA6060 aluminum extrusions	QS and D
2000	Seitzberger et al. [9]	Aluminum foam-filled monotubal and bitubal steel profiles	QS
2006	Kavi et al. [10]	Foam-filled thin-walled circular aluminum tube	QS
<i>Mainly by theoretical analysis</i>			
1988	Abramowicz and Wierzbicki [11]	Foam-filled prismatic columns	QS
2006, 2007	Wang et al. [12,13]	Aluminum foam-filled single hat and double hat sections	QS and D
2011	Mahmoudabadi and Sadighi [14]	Foam-filled metal hexagonal honeycomb	QS and D
<i>Mainly by numerical simulation</i>			
2009	Ahmad and Thambiratnam [15]	Metallic foam-filled conical tubes	QS
2008	Aktay et al. [16]	Aluminum and polystyrene foam-filled aluminum single, bitubular and multi-tube-packed (hexagonal and square packing) configurations	QS
2008	Mirfendereski et al. [17]	Foam-filled tapered thin-walled rectangular tubes	QS and D
2004	Meguid et al. [18]	PVC foam-filled thin-walled circular tubes	QS
2007	Shahbeyk et al. [19]	Aluminum foam-filled square columns	D

^a QS and D mean quasi-static and dynamic loading conditions, respectively.

[30] investigated the energy absorption characteristics of FGF-filled tubes in comparison with the UF-filled tubes and implemented crashworthiness optimization for these FGF-filled tubes. The density of the filled foams of their studied FGF-filled tubes changes along the axial direction of the tube. Nouraei [31] employed nonlinear finite element code LS-DYNA to investigate of the crush behavior of FGF-filled columns. He studied crashworthiness the FGF-filled columns, in which the foam density changes along both the axial and lateral directions of the column. However, previous studies on FGF-filled thin-walled structures did not considered various lateral graded conditions such as changing the foam density along the radius or the side of the section of the tube. Moreover, the characteristic of bond between the FGF materials and the tube wall was not considered.

In this paper, the energy absorption characteristics of two kinds of functionally lateral graded foam-filled tubes (FLGFTs) including bonded and non-bonded cases are firstly investigated by nonlinear finite element analysis through LS-DYNA. Then, the two kinds of FLGFTs are optimized by adopting multiobjective particle swarm optimization (MOPSO) algorithm to achieve maximum SEA and minimum peak crushing force (PCF). The optimal designs of FLGFTs that may provide an extremely excellent crashworthiness performance can be obtained.

2. Structural crashworthiness indicators

In order to evaluate the crashworthiness of the thin-walled structures, it is essential to define the crashworthiness indicators. Energy absorption (EA), specific energy absorption (SEA), mean crushing force (MCF) and crash load efficiency (CLE) are usually used as the important indicators for evaluating the crashworthiness. The energy absorption of a structure subjected to the axial loading can be expressed as:

$$EA(d) = \int_0^d F(x)dx, \quad (1)$$

where d is the axial crushing distance and F denotes the axial crushing force. The axial crushing force–displacement curve of a typical thin-walled structure is shown in Fig. 1. The mean crushing force for a given deformation can be calculated as:

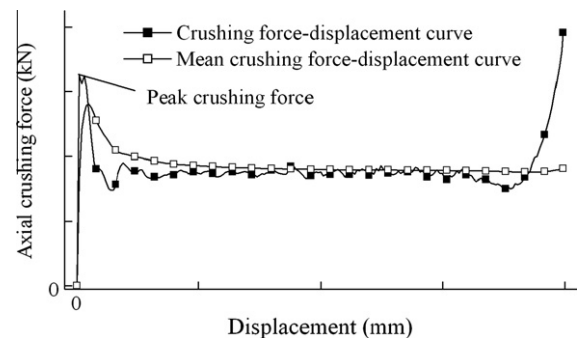


Fig. 1. Axial crushing force–displacement curves of a typical thin-walled structure.

$$MCF(d) = \frac{EA(d)}{d}. \quad (2)$$

The specific energy absorption is defined as the ratio of the absorbed energy to the mass of the structure. So it can be written as [32]:

$$SEA(d) = \frac{EA(d)}{M}, \quad (3)$$

where M is the mass of the structure. Apparently, the higher the SEA, the better the energy absorption capacity of a structure. As an energy absorber, the structure with high CLE is preferred in engineering [21]. CLE of a thin-walled structure can be given as [21]:

$$CLE = \frac{MCF}{PCF} \times 100\%, \quad (4)$$

where PCF represents the peak crushing force of a thin-walled structure, which is shown in Fig. 1.

3. Finite element modeling

3.1. Finite element model

The geometrical configuration of the structure considered in this study is shown in Fig. 2, which is actually a thin-walled square

tube filled with functionally graded aluminum foam. It is also shown in Fig. 2 that the sectional dimension and the length of the tube are 80 mm × 80 mm × 2 mm and 240 mm, respectively. The geometry of the tube is determined from the dimensions of a typical lower rail of a passenger car [32]. In order to simulate the front crash of a passenger car, the functionally lateral graded foam-filled tube (FLGFT) impacts onto a rigid wall at an initial velocity of 15 m/s with an additional mass of 600 kg attached to its right end in this study as shown in Fig. 2.

The tube is modeled using Belytschko–Tsai four-node shell elements with three integration points through the thickness and one integration point in the element plane. The functionally lateral graded foam (FLGF) is meshed with eight-node solid elements with one-point reduced integration. An automatic node-to-surface contact is chosen to simulate the contact between the specimen and the rigid wall. An automatic single-surface contact is adopted to simulate the buckling of the FLGF and the tube under axial dynamic loading. In these contacts, the static and dynamic coefficients of frictions are 0.20 [33]. In this study, two different adhesive conditions between the FLGF and the tube are considered. One is no adhesive bonding, the other is strong adhesive bonding. The interfaces between the FLGFs and the tubes are simulated using a surface-to-surface sliding contact model and a tiebreak-contact model in the non-bonded and bonded cases, respectively. In the tiebreak-contact model, sliding is not allowed from node to node until the tensile or shear stress exceeds the ultimate strength. But if the tensile or shear stress exceeds the tensile and shear ultimate strength, the bonding will fail and the contact will automatically behave as a surface-to-surface contact. The failure is determined by the following criterion [34,35]:

$$\left[\frac{\sigma}{\sigma_f}\right]^2 + \left[\frac{\tau}{\tau_f}\right]^2 \leq 1, \quad (5)$$

where σ_f and τ_f are tensile and shear ultimate strength of the adhesive material, respectively. In this study, $\sigma_f = 150$ MPa and $\tau_f = 150$ MPa [36].

From the above described finite element modeling method, the three dimensional finite element model of FLGFT is established by employing the explicit nonlinear finite element software LS-DYNA as shown in Fig. 3.

3.2. Material properties

The material of the tube here is aluminum alloy AA6060 T4 with mechanical properties of density $\rho = 2.7 \times 10^3$ kg/m³, Young's modulus $E = 68.2$ GPa, initial yield stress $\sigma_y = 80$ MPa, ultimate stress $\sigma_u = 173$ MPa, Poisson's ratio $\mu = 0.3$ and power law exponent $n = 0.23$ [6]. The constitutive behavior of the tube is based on an elastic–plastic material model with Von Mises's isotropic plasticity algorithm. In this material constitutive model, plastic hardening is defined by several piecewise lines. In order to define the piecewise lines, the pairs of the plastic strain and the true

stress should be specified, which are given in Table 2. The effect of strain rate in this model is neglected due to the insensitivity of strain rate of aluminum alloy material [37].

Functionally lateral graded foam (FLGF) is a new kind of filler material. In order to enhance the crashworthiness of aluminum alloy tube, it is filled with FLGF whose direction of density gradient is perpendicular to the axial impact velocity. In this study, the density gradient is determined by the following power-law function as [26,30]:

$$\rho_f(x) = \rho_{f1} + (\rho_{f2} - \rho_{f1}) \left(\frac{x}{l}\right)^m, \quad (6)$$

where ρ_{f1} and ρ_{f2} are the densities of outermost layer and innermost layer of the FLGF, respectively. As shown in Fig. 4, x is the distance from the outer side of the FLGF and l is the half width of the tube. m is the graded parameter that governs the variation of foam density. In the following study, two different kinds of FLGF shown as type A and type B in Fig. 4 are investigated. Type A-FLGFT represents one kind of typical functionally lateral graded foam-filled tube in which the foam density changes along the radial direction of the section of the tube. Type B-FLGFT is another typical one in which the foam density changes along the one-side direction of the section of the tube. However, there is no effective constitutive model available for functionally graded foam materials. In order to deal with this problem, the foam is divided into several layers along the direction of grading [30]. Each layer is considered as an isotropic uniform foam material whose constitutive behavior is based on as an isotropic uniform material model developed by Deshpande and Fleck [38]. The yield criterion of this material is defined as

$$\Phi = \sigma_e - Y \leq 0, \quad (7)$$

where Φ denotes the yield surface. Y is the yield strength and σ_e is an equivalent stress, which is given as

$$\sigma_e^2 = \frac{1}{1 + (\alpha/3)^2} (\sigma_v^2 + \alpha^2 \sigma_m^2), \quad (8)$$

where σ_v and σ_m represent the Von Mises effective stress and the mean stress, respectively. α is a parameter which can determine the shape of the yield surface and it can be written as

$$\alpha^2 = \frac{9(1 - 2\nu^p)}{2(1 + \nu^p)}, \quad (9)$$

where ν^p is the plastic coefficient of contraction. For the aluminum foam, $\nu^p = 0$ in most cases, then $\alpha = 2.12$.

The strain hardening rule is adopted in this material model as

$$Y = \sigma_p + \gamma \frac{\varepsilon_e}{\varepsilon_D} + \alpha_2 \ln \left[\frac{1}{1 - (\varepsilon_e/\varepsilon_D)^\beta} \right], \quad (10)$$

where ε_e is the equivalent strain. σ_p , α_2 , γ , β and ε_D are material parameters and can be expressed as functions of the foam density

$$\begin{cases} (\sigma_p, \alpha_2, \gamma, \frac{1}{\beta}, E_p) = C_0 + C_1 \left(\frac{\rho_f}{\rho_{f0}}\right)^q, \\ \varepsilon_D = -\frac{9+\alpha^2}{3\alpha^2} \ln \left(\frac{\rho_f}{\rho_{f0}}\right), \end{cases} \quad (11)$$

where ρ_f and ρ_{f0} denote the foam density and the base material density, respectively. C_0 , C_1 and q are constants, which are given in Table 3. It can be found from Eq. (11) that E_p is also a function of the foam density.

Fracture is considered in this model by removing (eroding) elements when they reach a critical strain. The volumetric strain ε_m , which is positive in tension and negative in compression, is chosen as a measure for when an element should be eroded. If $\varepsilon_m \geq \varepsilon_m^c$, the element will be eroded. ε_m^c means the critical volumetric strain and is defined as 0.1 in the study [37].

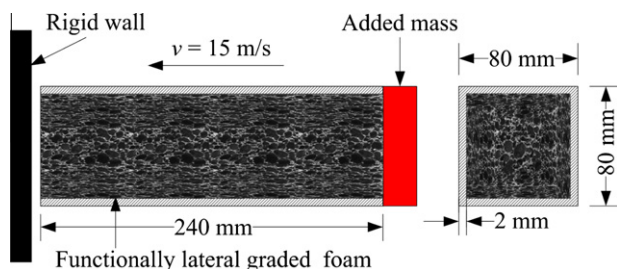


Fig. 2. Geometrical configuration and dimensions of FLGFT and its loading condition.

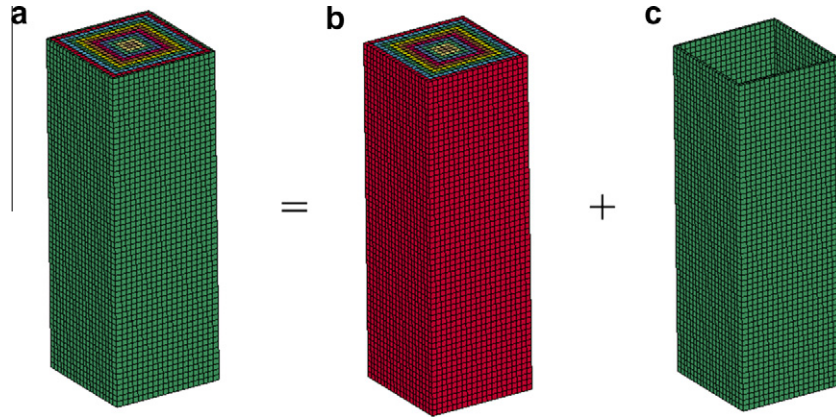


Fig. 3. Finite element model of FLGFT: (a) FLGFT, (b) FLGF filler and (c) tube.

Table 2
Strain hardening data for AA 6060 T4 [6].

Plastic strain (%)	Plastic stress (MPa)
0.0	80
2.4	115
4.9	139
7.4	150
9.9	158
12.4	167
14.9	171
17.4	173

4. Numerical simulation results and discussion

4.1. Validation of the finite element model

From Eq. (6), it can be easily found that the FLGFT will become a uniform foam-filled tube when the parameter m equals to 0. So the numerical results of FLGFT in this special case can be validated by employing a close-form formula of the mean crushing force, which was first developed by Hanssen et al. [8] based on experimental studies on the crash behaviors of uniform density foam-filled tube under the axial dynamic loading. This close-form formula for the mean crushing force can be written as

$$F_{mean} = 13.06\sigma_0 b_m^{1/3} t^{5/3} \left[1 + C_{ine} \left(\frac{b_m \rho v_0^2}{t \sigma_0} \right)^{1/2} \right] + \sigma_p b_i^2 + C_{mean} \sqrt{\sigma_p \sigma_0} b_m t, \quad (12)$$

where σ_0 represents the characteristic stress of the tube material, b_m the inner cross-section width, t the thickness of the tube wall, ρ the density of the tube material, σ_p the foam plateau stress, and v_0 is the initial impact velocity. C_{mean} is the interaction constant and is a function of the relative deformation D_c , which is defined as the ratio of the deformed distance d to the original length of the tube l . C_{ine} is the dynamic amplification constant and is a function of relative lobe length d/H , where d is the deformation and H is the half natural lobe length of non-filled tube. The half natural lobe length H was deduced by Abromowicz and Jones [41] as

$$H = 0.99 b_m^{2/3} t^{1/3}. \quad (13)$$

The comparison of the mean crushing force versus displacement of the FLGFTs ($m = 0$) between the finite element analysis (FEA) and empirical solutions with $\rho_f = 0.3, 0.4$ and 0.5 g/cm^3 are shown in Fig. 5. It can be found that the FEA results are in good agreement with the empirical solutions. This satisfactory correlation provides adequate evidence for extending the uniform foam-filler model ($m = 0$) to the FLGF filler models (m equals any other values), which will be used in the following study.

4.2. Crashworthiness comparison of uniform foam and type A-FLGF filled tubes

In order to compare the energy absorption capacity of uniform foam-filled tubes (UFT) with that of FLGFTs with the same weight, numerical simulations are implemented based on the finite element models of the FLGFTs with different values of parameter m . In this study, the values of parameter m are chosen as 0, 0.1, 0.2, ..., 0.9, 1, 2, ..., 9, 10, which correspond to 21 different

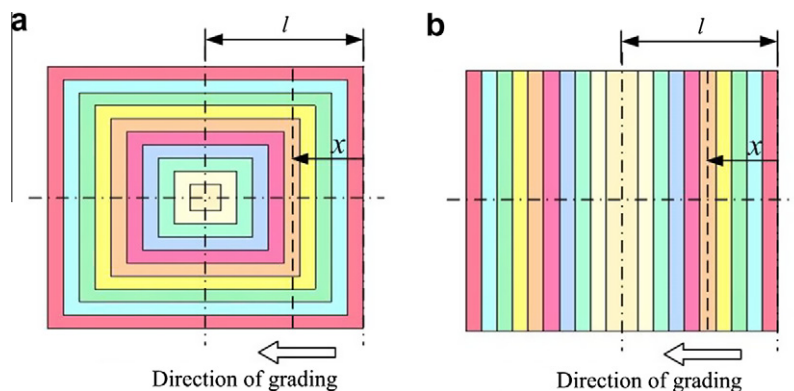


Fig. 4. Design parameters for FLGFs: (a) Top view of FLGF of type A and (b) Top view of FLGF of type B.

Table 3
Material constants for aluminum foam [39,40].

	σ_p (MPa)	α_2 (MPa)	$1/\beta$	γ (MPa)	E_p (MPa)
C_0 (MPa)	0	0	0.22	0	0
C_1 (MPa)	720	140	320	42	0.33×10^6
q	2.33	0.45	4.66	1.42	2.45

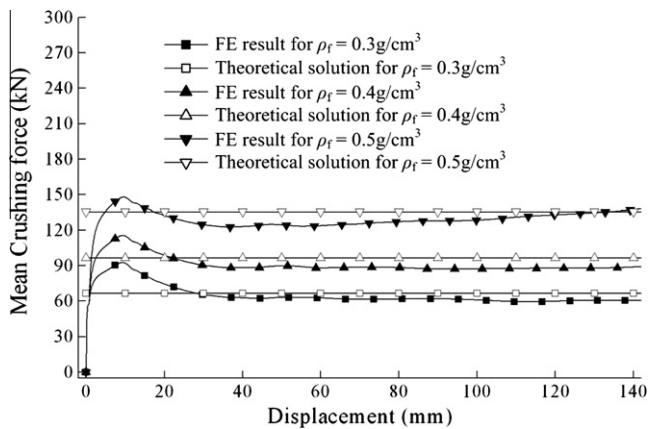


Fig. 5. Mean crushing force versus displacement of the FLGFTs ($m = 0$).

cases. In each case, the thickness of the tube is 2.0 mm and the deformation of the FLGFT is 120 mm. To be consistent, $\rho_{f1} = 0.5 \text{ g/cm}^3$ and $\rho_{f2} = 0.3 \text{ g/cm}^3$ for all the FLGFTs. In order to keep the same weight as the FLGFT, the foam density of UFT will vary with the value of parameter m . Hence, the foam density of UFT can also be expressed in term of the parameter m . It is easy to find that the foam densities of UFTs decrease with decreasing m . The lowest density of the foam is 0.3 g/cm^3 when m equals to 0. In order to consider the effect of the bond between foam and inner wall of the tube, FLGFTs with no bonding and strong bonding are investigated.

The relationship of EA versus m of type A-FLGFTs and the corresponding UFTs are presented in Fig. 6. It can be seen from Fig. 6 that EA of the type A-FLGFT is greater than that of the corresponding UFT, and EA of the FLGFT (or UFT) with bonding is obviously much greater than that of the FLGFT (or UFT) without bonding. Fig. 7 shows the relationship between SEA and m of the type A-FLGFT and the corresponding UFT. It is generally the same as Fig. 6 that SEA of the type A-FLGFT is bigger than that of the corre-

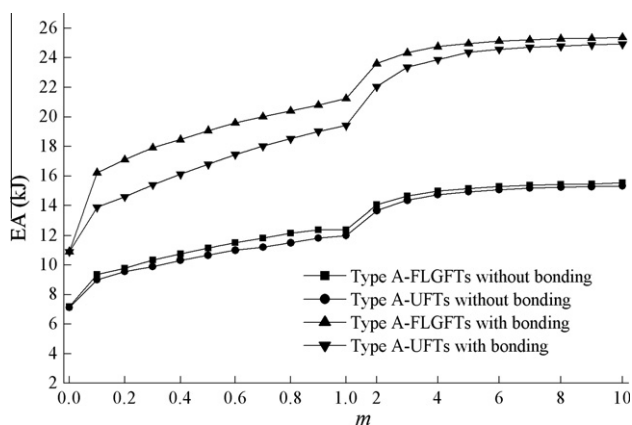


Fig. 6. EA versus m of the type A-FLGFTs and the corresponding UFTs.

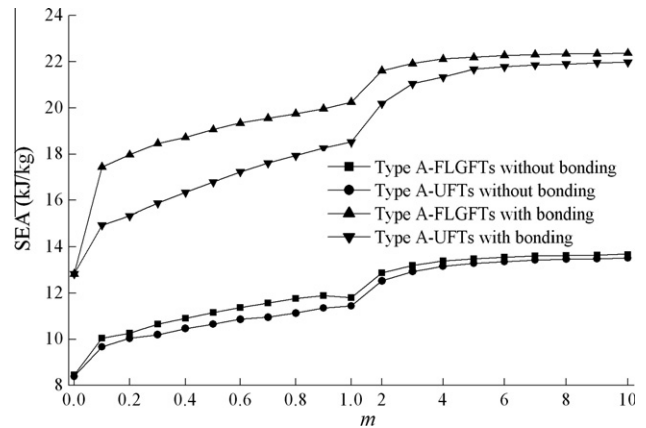


Fig. 7. SEA versus m of the type A-FLGFTs and the corresponding UFTs.

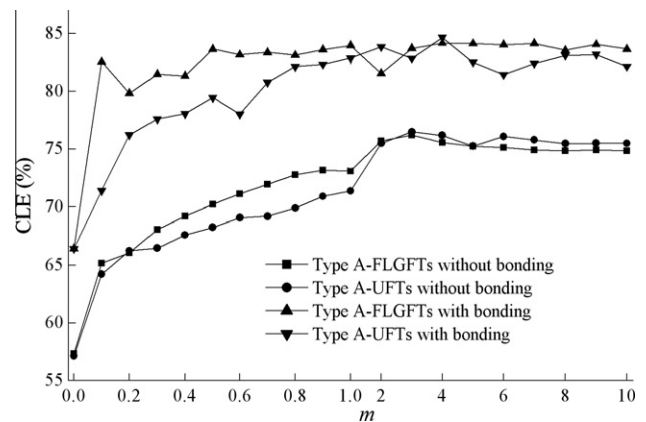


Fig. 8. CLE versus m of the type A-FLGFTs and the corresponding UFTs.

sponding UFT. And, SEA of the FLGFT (or UFT) with bonding is apparently much bigger than that of the FLGFT (or UFT) without bonding. According to Figs. 6 and 7, it can be easily found that both of EA and SEA increase monotonously for type A-FLGFTs and the corresponding UFTs. Fig. 8 plots the relationship between CLE and m . It can be seen from Fig. 8 that CLE of the type A-FLGFT with bonding is obviously greater than that of the corresponding UFT except for the cases of $m = 2$ and 4. It can be found from Fig. 8 that CLE of the type A-FLGFT without bonding is larger than or almost the same as that of the corresponding UFT when m is less than 1. However, an opposite result can be observed when m is larger than 1 for the cases without bonding. The above results indicate that the crashworthiness of type A-FLGFT is generally better than that of the UFT in terms of the crashworthiness indicators of EA, SEA and CLE, especially for the case with bonding.

4.3. Crashworthiness comparison of uniform foam and type B-FLGF filled tubes

Fig. 9 shows the relationships of EA versus m of the type B-FLGFTs and the corresponding UFTs. According to Fig. 9, it can be found that EA of the type B-FLGFT is greater than or almost the same as that of the corresponding UFT. Moreover, EA of the FLGFT (or UFT) with bonding is obviously much greater than that of the FLGFT (or UFT) without bonding. Fig. 10 gives the relationship between SEA and m for the type B-FLGFTs and the corresponding UFTs. It can be found that SEA of the type B-FLGFT is bigger than or almost the same as that of the corresponding UFT. In addition, SEA of the FLGFT (or UFT) with bonding is obviously much

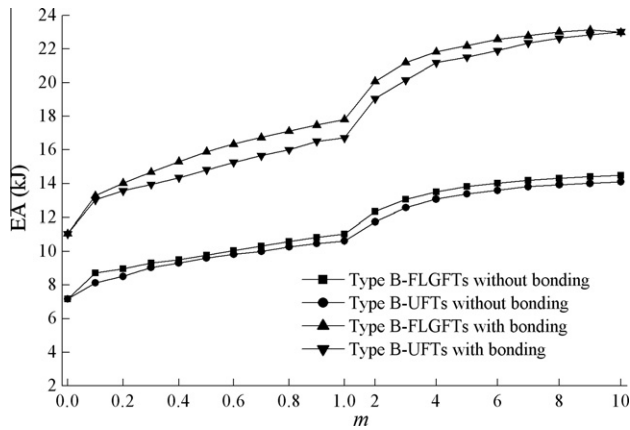


Fig. 9. EA versus m of the type B-FLGFTs and the corresponding UFTs.

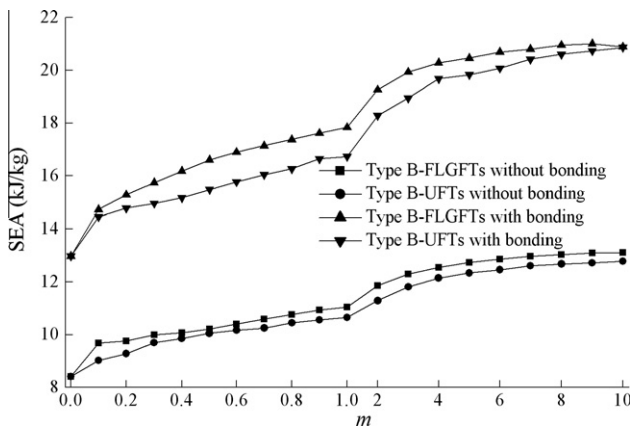


Fig. 10. SEA versus m of the type B-FLGFTs and the corresponding UFTs.

bigger than that of the FLGFT (or UFT) without bonding. From Figs. 9 and 10, it can be easily found that both of EA and SEA monotonously increase with the increase of parameter m for type B-FLGFTs and the corresponding UFTs. Fig. 11 plots the relationship between CLE and m , from which it can be seen that CLE of the type B-FLGFT with bonding is obviously greater than that of the corresponding UFT. In addition, it can be found from Fig. 11 that CLE of the type B-FLGFT without bonding is larger than or almost the same as that of the corresponding UFT. Based on the above results, it can be found that the crashworthiness of type B-FLGFT is obviously better

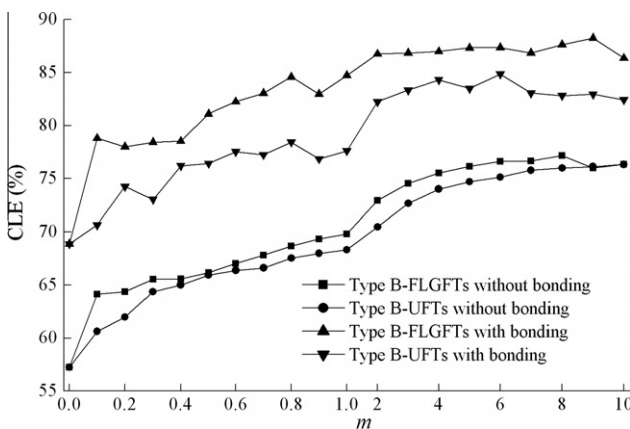


Fig. 11. CLE versus m of the type B-FLGFTs and the corresponding UFTs.

than that of the UFT in terms of the crashworthiness indicators of EA, SEA and CLE, especially for the case with bonding.

Based on the above comparison results, the FLGFTs of type A and type B have a more excellent crashworthiness than the corresponding UFTs in general. Thus, the FLGFTs can be used as good energy absorbers in the vehicle engineering in future. However, it can be found from the above study that the graded parameter m gives rise to significant influence on the crashworthiness of FLGFTs. Therefore, it is of great importance to seek the best value of parameter m to optimize the crashworthiness of the FLGFTs, which is presented in the next section.

5. Multiobjective optimization design

5.1. Methodology

As an energy absorber, the structure is expected to absorb as much impact energy as possible per unit mass. Thus, SEA should be chosen as an objective function and maximized in the crashworthiness optimization problem. On the other hand, PCF of the structure is another very importance indicator for the safety of the cushioned object. PCF of the structure should be constrained under a certain level. Thus, PCF is set as another objective function and minimize it in the optimization problem. To account for these two different design criteria, the optimization problem can be written as the following multiobjective optimization form:

$$\begin{cases} \text{Minimize} & [\text{PCF}(m), -\text{SEA}(m)] \\ \text{Subject to} & m^L \leq m \leq m^U \end{cases} \quad (14)$$

where m is the gradient parameter, m^L and m^U are the lower limit and upper limit of parameter m , respectively. In this paper, m^L and m^U are selected as 0 and 10, respectively. The flowchart of the implementation of the multiobjective optimization design (MOD) in this study is shown in Fig. 12 [42].

Design of experiment (DOE) method provides a means of selection of the sampling points in the design space in a more efficient way. Many different experimental design methods can be used for sampling points in the design space [43,44]. The full factorial design method is used to sample the design points in this paper for the advantage of its uniformity [45]. In this paper, 11 experimental design points are obtained using the full factorial design method for the design spaces of 0–1 and 1–10 of the design variable m , respectively. In the flowchart of the entire multiobjective optimization design, the main time-consuming part is FEA. In this study, the FEA process cost about 1.5 h with a computer of Inter (R) Core (TM) 2 Quad CPU Q9400 @ 2.66 GHz for each case which corresponds to one experimental design point. Thus, it will cost about 31.5 h for the multiobjective optimization of each kind of foam-filled tube.

Metamodels are usually used in the optimization problems in modern industry. In this study, the metamodels of the objective functions are constructed using polynomial functions [46,47]. Based on the developed metamodels, the objective function values in the design space can be easily calculated. In order to evaluate the accuracies of the developed metamodels, the relative error (RE) between the FEA result $y(\mathbf{x})$ and the approximation based on the regression function $\hat{y}(\mathbf{x})$ is calculated as

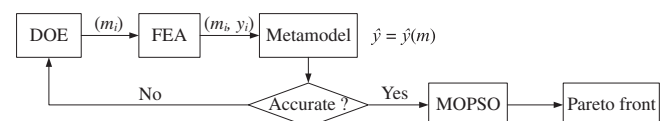


Fig. 12. Flowchart of the implementation of MOD.

Table 4

Accuracies of the metamodels for the type A-FLGFTs and the corresponding UFTs.

Metamodel	Order	R^2	RMSE	MAX	RE (%)
<i>Without bonding</i>					
$SEA_{NB}^G(m)$ ($0 \leq m \leq 1$)	1	0.8311	0.4414	1.0362	[−12.2466, 2.9903]
	2	0.9440	0.2695	0.4992	[−5.6924, 4.9649]
	3	0.9627	0.2352	0.4589	[−3.3102, 4.5639]
	4	0.9870	0.1499	0.2806	[−1.5339, 2.7911]
	5	0.9925	0.1246	0.1766	[−1.7204, 1.6491]
	6	0.9973	0.0835	0.1155	[−1.1250, 0.6432]
	7	0.9991	0.0551	0.0611	[−0.4933, 0.5731]
$SEA_{NB}^G(m)$ ($1 \leq m \leq 10$)	1	0.6459	0.3661	0.7929	[−6.7191, 2.4829]
	2	0.8926	0.2155	0.3415	[−2.8942, 2.0904]
	3	0.9743	0.1139	0.1938	[−0.9835, 1.5063]
	4	0.9933	0.0636	0.0951	[−0.3515, 0.7389]
	5	0.9989	0.0293	0.0376	[−0.2850, 0.2336]
	6	0.9997	0.0163	0.0176	[−0.1337, 0.1257]
	7	0.9999	0.0128	0.0115	[−0.0809, 0.0859]
$PCF_{NB}^G(m)$ ($0 \leq m \leq 1$)	1	0.8732	4.1629	9.8444	[−9.4268, 2.2640]
	2	0.9585	2.5269	4.5999	[−4.4047, 3.5869]
	3	0.9759	2.0564	3.8651	[−2.3719, 3.2319]
	4	0.9923	1.2604	2.2756	[−0.8901, 1.9029]
	5	0.9968	0.8936	1.1451	[−0.8495, 0.9575]
	6	0.9994	0.4137	0.5483	[−0.4452, 0.2684]
	7	0.9999	0.2356	0.2251	[−0.1686, 0.1780]
$PCF_{NB}^G(m)$ ($1 \leq m \leq 10$)	1	0.7724	5.1177	10.2772	[−7.2805, 3.0355]
	2	0.9637	2.1844	3.3465	[−2.3707, 1.6717]
	3	0.9942	0.9454	1.7849	[−0.6698, 1.1542]
	4	0.9976	0.6664	1.0556	[−0.5032, 0.6826]
	5	0.9989	0.5125	0.7675	[−0.4790, 0.3321]
	6	0.9993	0.4742	0.5287	[−0.3300, 0.2709]
	7	0.9998	0.3112	0.2772	[−0.1209, 0.1677]
$SEA_{NB}^U(m)$ ($0 \leq m \leq 1$)	1	0.8602	0.3482	0.8420	[−10.0332, 3.1186]
	2	0.9385	0.2450	0.4417	[−5.2636, 3.5971]
	3	0.9741	0.1699	0.2995	[−2.3849, 3.0974]
	4	0.9905	0.1114	0.1727	[−1.4204, 1.7865]
	5	0.9960	0.0794	0.0785	[−0.7697, 0.7572]
	6	0.9998	0.0218	0.0202	[−0.1961, 0.1932]
	7	0.9998	0.0251	0.0211	[−0.1955, 0.2014]
$SEA_{NB}^U(m)$ ($1 \leq m \leq 10$)	1	0.6743	0.3901	0.8276	[−7.2313, 2.7496]
	2	0.9165	0.2112	0.3308	[−2.8902, 1.9602]
	3	0.9821	0.1055	0.1707	[−0.9273, 1.3624]
	4	0.9966	0.0504	0.0750	[−0.3118, 0.5988]
	5	0.9995	0.0223	0.0292	[−0.2261, 0.1842]
	6	0.9998	0.0156	0.0155	[−0.1197, 0.0737]
	7	1.0000	0.0079	0.0070	[−0.0390, 0.0524]
$PCF_{NB}^U(m)$ ($0 \leq m \leq 1$)	1	0.9117	3.4407	8.0243	[−7.7180, 2.0521]
	2	0.9751	1.9379	3.5452	[−3.4098, 2.7960]
	3	0.9875	1.4690	2.9068	[−1.7072, 2.4924]
	4	0.9950	1.0037	1.8388	[−0.6800, 1.5767]
	5	0.9979	0.7117	0.9385	[−0.7780, 0.8047]
	6	0.9994	0.4169	0.5640	[−0.4693, 0.2781]
	7	0.9998	0.2516	0.2588	[−0.1893, 0.2087]
$PCF_{NB}^U(m)$ ($1 \leq m \leq 10$)	1	0.8008	4.4685	8.5029	[−6.0674, 3.4078]
	2	0.9725	1.7756	2.3753	[−1.6949, 1.0832]
	3	0.9942	0.8823	1.1576	[−0.7017, 0.6657]
	4	0.9955	0.8500	1.3588	[−0.4918, 0.8213]
	5	0.9955	0.9503	1.3540	[−0.4889, 0.8184]
	6	0.9961	1.0236	1.1409	[−0.6181, 0.6896]
	7	0.9984	0.7997	0.6932	[−0.3467, 0.4190]
<i>Bonding</i>					
$SEA_B^G(m)$ ($0 \leq m \leq 1$)	1	0.6550	1.2766	3.1407	[−24.4789, 5.5400]
	2	0.8235	0.9686	1.7702	[−13.7969, 8.6750]
	3	0.9229	0.6844	1.3245	[−6.4584, 7.5952]
	4	0.9687	0.4707	0.8291	[−2.5972, 4.7544]
	5	0.9911	0.2745	0.3602	[−2.0013, 2.0657]
	6	0.9977	0.1562	0.2150	[−1.1965, 0.6928]
	7	0.9993	0.1001	0.1136	[−0.5124, 0.6155]
$SEA_B^G(m)$ ($1 \leq m \leq 10$)	1	0.5791	0.4467	0.9867	[−4.8718, 1.7650]
	2	0.8533	0.2819	0.4540	[−2.2418, 1.8007]
	3	0.9552	0.1683	0.2953	[−0.8502, 1.3661]
	4	0.9871	0.0991	0.1522	[−0.3525, 0.7044]

Table 4 (continued)

Metamodel	Order	R^2	RMSE	MAX	RE (%)
$PCF_B^C(m)$ ($0 \leq m \leq 1$)	5	0.9971	0.0526	0.0703	[−0.3206, 0.2520]
	6	0.9991	0.0333	0.0361	[−0.1646, 0.1488]
	7	0.9997	0.0239	0.0214	[−0.0917, 0.0968]
	1	0.8486	8.9029	20.4797	[−14.9864, 5.2332]
	2	0.9420	5.8443	9.7366	[−7.1250, 4.8320]
	3	0.9827	3.4158	4.4660	[−2.4858, 2.2281]
	4	0.9973	1.4488	1.6619	[−0.9071, 0.7187]
$PCF_B^C(m)$ ($1 \leq m \leq 10$)	5	0.9986	1.1444	1.5172	[−0.7986, 0.7055]
	6	0.9988	1.2096	1.4295	[−0.6329, 0.7554]
	7	0.9988	1.3967	1.4418	[−0.6329, 0.7619]
	1	0.5749	8.5402	19.3958	[−9.2013, 3.3119]
	2	0.7916	6.3919	10.9932	[−4.9282, 4.5563]
	3	0.8962	4.8737	9.1828	[−2.3517, 3.8060]
	4	0.9538	3.5617	5.5243	[−1.2348, 2.2896]
$SEA_B^C(m)$ ($0 \leq m \leq 1$)	5	0.9864	2.1566	2.7513	[−1.1358, 0.8987]
	6	0.9941	1.6482	1.5244	[−0.6162, 0.6046]
	7	0.9996	0.5142	0.4259	[−0.1633, 0.1710]
	1	0.9181	0.5116	1.2358	[−9.6317, 2.5774]
	2	0.9668	0.3457	0.6299	[−4.9097, 4.1993]
	3	0.9807	0.2813	0.5693	[−2.6457, 3.8105]
	4	0.9910	0.2076	0.3765	[−1.1425, 2.5197]
$SEA_B^U(m)$ ($1 \leq m \leq 10$)	5	0.9967	0.1376	0.1865	[−1.2162, 1.2182]
	6	0.9990	0.0850	0.1163	[−0.7583, 0.4403]
	7	0.9996	0.0584	0.0563	[−0.3368, 0.3546]
	1	0.6795	0.6593	1.3512	[−7.2933, 2.7556]
	2	0.9317	0.3253	0.4872	[−2.6300, 2.0419]
	3	0.9891	0.1405	0.1806	[−0.6993, 0.8946]
	4	0.9977	0.0708	0.1224	[−0.5740, 0.2722]
$PCF_B^U(m)$ ($0 \leq m \leq 1$)	5	0.9990	0.0520	0.0754	[−0.3535, 0.2190]
	6	0.9992	0.0552	0.0658	[−0.3085, 0.2608]
	7	0.9993	0.0606	0.0554	[−0.2598, 0.2238]
	1	0.9015	5.8360	12.6661	[−9.2687, 4.8066]
	2	0.9438	4.6773	10.1438	[−4.9712, 6.2552]
	3	0.9496	4.7336	9.7533	[−3.5424, 6.0144]
	4	0.9572	4.7123	8.0294	[−2.2808, 4.9513]
$PCF_B^U(m)$ ($1 \leq m \leq 10$)	5	0.9801	3.5228	4.0533	[−2.5397, 2.4520]
	6	0.9925	2.4155	2.9376	[−1.6674, 0.9980]
	7	0.9931	2.6806	2.9376	[−1.6674, 1.2857]
	1	0.7123	10.4416	19.8429	[−10.1573, 4.2526]
	2	0.9411	5.0495	7.3075	[−3.1163, 3.1092]
	3	0.9797	3.2051	6.0551	[−2.5768, 1.3714]
	4	0.9799	3.4940	6.0118	[−2.5584, 1.2670]
	5	0.9874	3.0918	4.1310	[−1.7580, 1.3398]
	6	0.9883	3.4429	3.7859	[−1.5953, 1.6108]
	7	0.9931	3.2250	2.8041	[−1.1933, 0.7878]

$$RE = \frac{y(\mathbf{x}) - \hat{y}(\mathbf{x})}{y(\mathbf{x})} \quad (15)$$

In addition, the accuracies of these metamodels can be evaluated based on the square value (R^2), the root mean square error (RMSE) and the maximum absolute error (MAX), respectively, which are written as

$$R^2 = 1 - \frac{SS_E}{SS_T} \quad (16)$$

$$RMSE = \sqrt{\frac{SS_E}{n-k-1}} \quad (17)$$

$$MAX = \max |y_i - \hat{y}_i|, \quad i = 1, 2, \dots, n, \quad (18)$$

where n is the number of sampling points and k is the number of non-consist terms in metamodel. MAX is used to gauge the local accuracy of the model, while RSME is used to gauge the overall accuracy of the model. The smaller the values of RSME and MAX, or the larger the value of R^2 , the more accurate the metamodel. SS_E and SS_T are the sum of squared errors and the total sum of squares, which can be calculated as:

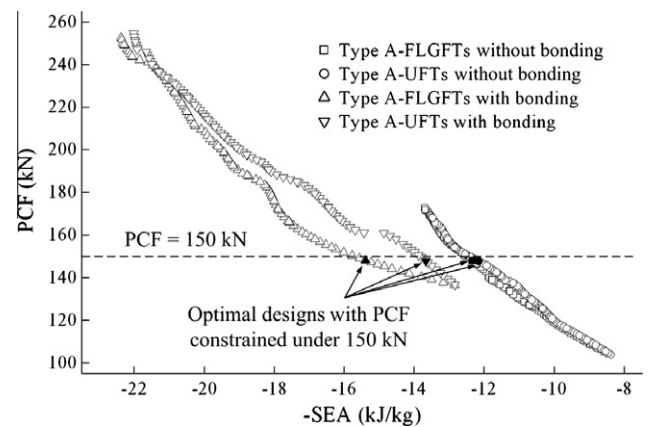


Fig. 13. Pareto fronts of the type A-FLGFTs and the corresponding UFTs.

$$SS_E = \sum_{i=1}^n (y_i - \hat{y}_i)^2 \quad (19)$$

$$SS_T = \sum_{i=1}^n (y_i - \bar{y})^2 \quad (20)$$

Table 5

Optimal solutions with PCF constrained under 150 kN.

	Optimal m	SEA (kJ/kg)			PCF (kN)		
		Metamodel	FEA	Error (%)	Metamodel	FEA	Error (%)
<i>Type A</i>							
FLGFTs (no bonding)	1.4992	12.4883	12.5085	−0.1615	149.8432	148.8150	0.6909
UFTs (no bonding)	1.7639	12.3638	12.3220	0.3392	149.7597	149.3070	0.3032
FLGFTs (bonding)	0.0384	15.5138	16.2956	−4.7976	149.0019	149.2391	−0.1589
UFTs (bonding)	0.0263	13.7385	14.3965	−4.5706	148.9693	149.1991	−0.1540
<i>Type B</i>							
FLGFTs (no bonding)	4.4408	12.6383	12.6361	0.0174	149.8328	149.9390	−0.0708
UFTs (no bonding)	5.2424	12.3662	12.3515	0.1190	149.6140	149.5940	0.0134
FLGFTs (bonding)	0.1958	15.2753	15.2692	0.0399	149.3940	149.0910	0.2032
UFTs (bonding)	0.0542	14.0209	14.0280	−0.0506	148.8519	149.8330	−0.6548

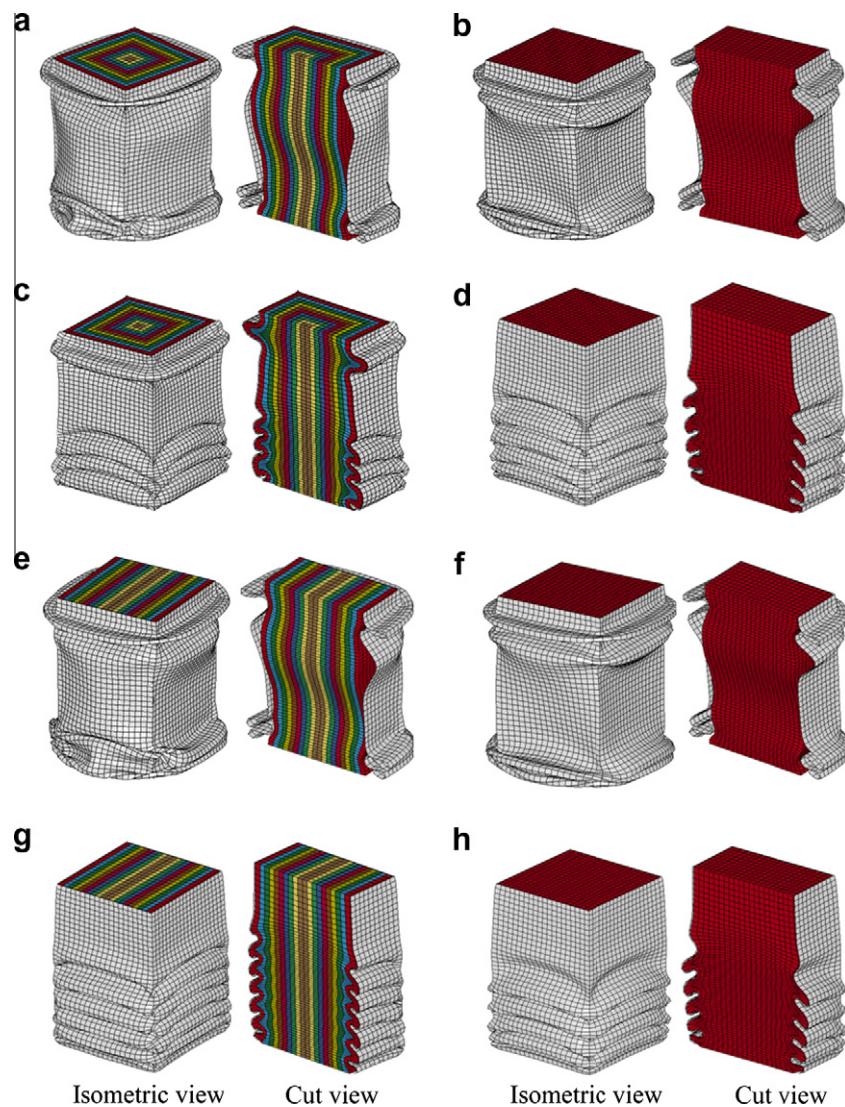


Fig. 14. Deformation profiles of optimal designs with PCF constrained under 150 kN: (a) type A-FLGFTs without bonding, (b) type A-UFTs without bonding, (c) type A-FLGFTs with bonding, (d) type A-UFTs with bonding, (e) type B-FLGFTs without bonding, (f) type B-UFTs without bonding, (g) type B-FLGFTs with bonding and (h) type B-UFTs with bonding.

where \bar{y} is the mean value of y_i .

In comparison with other multiobjective optimization algorithms such as NSGA [48] and PEAS approaches [49,50], the multiobjective particle swarm optimization (MOPSO) that incorporates the mechanism of crowding distance computation has drawn con-

siderable attention recently due to its relatively fast convergence and well-distributed Pareto front. The details of MOPSO can be consulted from Ref. [49]. In this paper, the MOPSO algorithm is employed to obtain the Pareto front of the two conflicting objectives of SEA and PCF. The Pareto front is actually a set of the

Table 6

Accuracies of the metamodels for the type B-FLGFTs and the corresponding UFTs.

Metamodel	Order	R^2	RMSE	MAX	RE (%)
<i>Without bonding</i>					
$SEA_{NB}^G(m)$ ($0 \leq m \leq 1$)	1	0.8583	0.2929	0.7203	[−8.5585, 3.4173]
	2	0.9055	0.2537	0.4606	[−5.4724, 4.4913]
	3	0.9461	0.2049	0.3914	[−2.9144, 4.0462]
	4	0.9815	0.1297	0.2356	[−1.2218, 2.4359]
	5	0.9927	0.0894	0.1390	[−1.4245, 1.2087]
	6	0.9963	0.0707	0.1004	[−1.0287, 0.6938]
	7	0.9981	0.0584	0.0665	[−0.5497, 0.6655]
$SEA_{NB}^G(m)$ ($1 \leq m \leq 10$)	1	0.8017	0.3134	0.6259	[−5.6681, 2.3433]
	2	0.9694	0.1316	0.2002	[−1.8129, 1.2560]
	3	0.9949	0.0581	0.0828	[−0.5076, 0.6984]
	4	0.9995	0.0192	0.0270	[−0.1396, 0.2277]
	5	1.0000	0.0067	0.0074	[−0.0606, 0.0555]
	6	1.0000	0.0037	0.0041	[−0.0316, 0.0222]
	7	1.0000	0.0028	0.0025	[−0.0189, 0.0189]
$PCF_{NB}^G(m)$ ($0 \leq m \leq 1$)	1	0.9332	2.2321	5.3097	[−5.0845, 1.3411]
	2	0.9775	1.3742	2.5174	[−2.4106, 1.9931]
	3	0.9890	1.0256	2.0025	[−1.1899, 1.7680]
	4	0.9955	0.7110	1.2643	[−0.5302, 1.1162]
	5	0.9986	0.4401	0.5741	[−0.4687, 0.5069]
	6	0.9997	0.2420	0.3088	[−0.2663, 0.1641]
	7	0.9999	0.1094	0.1104	[−0.0845, 0.0932]
$PCF_{NB}^G(m)$ ($1 \leq m \leq 10$)	1	0.8616	3.2443	6.6881	[−5.0821, 2.1521]
	2	0.9611	1.8381	2.6244	[−1.9942, 1.4008]
	3	0.9903	0.9901	1.6071	[−0.5511, 1.0167]
	4	0.9968	0.6203	1.0182	[−0.6585, 0.4989]
	5	0.9969	0.6874	1.0117	[−0.6542, 0.4407]
	6	0.9984	0.5752	0.6429	[−0.4158, 0.4007]
	7	0.9992	0.4881	0.4414	[−0.2230, 0.2862]
$SEA_{NB}^U(m)$ ($0 \leq m \leq 1$)	1	0.9187	0.2098	0.4294	[−5.1024, 2.5590]
	2	0.9850	0.0956	0.1383	[−1.6439, 1.3586]
	3	0.9959	0.0534	0.0762	[−0.7170, 0.8442]
	4	0.9966	0.0524	0.0875	[−0.9436, 0.6114]
	5	0.9967	0.0571	0.0865	[−0.9328, 0.6781]
	6	0.9973	0.0570	0.0708	[−0.7626, 0.6486]
	7	0.9982	0.0535	0.0610	[−0.4720, 0.6289]
$SEA_{NB}^U(m)$ ($1 \leq m \leq 10$)	1	0.8358	0.3021	0.5427	[−5.0961, 2.6044]
	2	0.9846	0.0988	0.1260	[−1.1061, 1.0669]
	3	0.9989	0.0289	0.0446	[−0.3578, 0.2625]
	4	0.9993	0.0258	0.0309	[−0.2739, 0.1812]
	5	0.9993	0.0269	0.0262	[−0.2106, 0.1967]
	6	0.9999	0.0114	0.0131	[−0.0855, 0.1040]
	7	0.9999	0.0139	0.0126	[−0.0906, 0.1002]
$PCF_{NB}^U(m)$ ($0 \leq m \leq 1$)	1	0.9466	1.8873	4.3834	[−4.1974, 1.2017]
	2	0.9855	1.0426	1.9082	[−1.8272, 1.4865]
	3	0.9934	0.7526	1.4621	[−0.8733, 1.3083]
	4	0.9974	0.5149	0.9155	[−0.3875, 0.8192]
	5	0.9992	0.3177	0.4148	[−0.3439, 0.3712]
	6	0.9998	0.1756	0.2247	[−0.1962, 0.1208]
	7	1.0000	0.0811	0.0810	[−0.0632, 0.0692]
$PCF_{NB}^U(m)$ ($1 \leq m \leq 10$)	1	0.8067	3.5878	7.1724	[−5.5298, 2.3016]
	2	0.9691	1.5334	2.3149	[−1.7848, 1.2300]
	3	0.9957	0.6208	0.9210	[−0.4698, 0.6625]
	4	0.9995	0.2409	0.3360	[−0.1509, 0.2417]
	5	0.9999	0.0825	0.0834	[−0.0579, 0.0568]
	6	1.0000	0.0202	0.0206	[−0.0143, 0.0120]
	7	1.0000	0.0128	0.0113	[−0.0076, 0.0070]
<i>Bonding</i>					
$SEA_B^G(m)$ ($0 \leq m \leq 1$)	1	0.8923	0.5040	1.1711	[−9.0274, 2.3537]
	2	0.9698	0.2829	0.5141	[−3.9628, 2.9785]
	3	0.9877	0.1929	0.3824	[−1.7870, 2.5954]
	4	0.9939	0.1468	0.2539	[−0.9137, 1.7230]
	5	0.9980	0.0929	0.1129	[−0.6076, 0.7662]
	6	0.9998	0.0337	0.0391	[−0.2556, 0.1617]
	7	1.0000	0.0140	0.0151	[−0.0866, 0.0960]
$SEA_B^G(m)$ ($1 \leq m \leq 10$)	1	0.7275	0.5482	1.1124	[−6.2361, 2.4352]
	2	0.9533	0.2427	0.3753	[−2.1040, 1.5199]
	3	0.9821	0.1623	0.2001	[−0.8225, 1.0387]
	4	0.9993	0.0362	0.0531	[−0.1493, 0.2568]

(continued on next page)

Table 6 (continued)

Metamodel	Order	R^2	RMSE	MAX	RE (%)
$PCF_B^C(m)$ ($0 \leq m \leq 1$)	5	0.9997	0.0275	0.0404	[−0.1083, 0.1951]
	6	0.9998	0.0261	0.0306	[−0.1348, 0.1478]
	7	0.9998	0.0300	0.0255	[−0.1099, 0.1233]
	1	0.9148	4.1825	6.4159	[−4.7948, 3.9305]
	2	0.9772	2.2927	3.4210	[−2.0299, 1.8966]
	3	0.9882	1.7620	2.6366	[−1.4545, 1.5021]
	4	0.9887	1.8638	2.9711	[−1.2162, 1.6927]
$PCF_B^C(m)$ ($1 \leq m \leq 10$)	5	0.9957	1.2605	1.8599	[−1.1036, 0.7098]
	6	0.9962	1.3282	1.6019	[−0.9505, 0.6985]
	7	0.9973	1.2926	1.2087	[−0.5749, 0.7448]
	1	0.7887	7.1333	14.0307	[−8.0099, 3.3686]
	2	0.9626	3.2099	4.4730	[−2.5536, 1.9877]
	3	0.9940	1.3909	1.9192	[−0.9060, 0.6871]
	4	0.9961	1.2336	1.6144	[−0.7216, 0.7384]
$SEA_B^U(m)$ ($0 \leq m \leq 1$)	5	0.9985	0.8628	0.7838	[−0.3700, 0.3507]
	6	0.9997	0.4125	0.4019	[−0.1837, 0.1829]
	7	0.9998	0.4429	0.3396	[−0.1175, 0.1624]
	1	0.9205	0.3210	0.7844	[−6.0102, 2.1697]
	2	0.9496	0.2711	0.4862	[−3.7252, 2.9945]
	3	0.9692	0.2267	0.3893	[−2.0481, 2.6918]
	4	0.9909	0.1329	0.2106	[−0.8699, 1.4562]
$SEA_B^U(m)$ ($1 \leq m \leq 10$)	5	0.9966	0.0892	0.1041	[−0.5250, 0.6255]
	6	0.9998	0.0250	0.0325	[−0.2000, 0.1462]
	7	0.9998	0.0250	0.0227	[−0.1275, 0.1417]
	1	0.8430	0.5470	1.1097	[−6.6322, 3.3309]
	2	0.9682	0.2630	0.3880	[−2.3192, 1.5756]
	3	0.9916	0.1464	0.1979	[−0.7385, 1.0826]
	4	0.9970	0.0954	0.1239	[−0.6538, 0.5656]
$PCF_B^U(m)$ ($0 \leq m \leq 1$)	5	0.9972	0.1024	0.1349	[−0.6425, 0.6852]
	6	0.9973	0.1180	0.1317	[−0.6700, 0.6694]
	7	0.9982	0.1185	0.1030	[−0.3590, 0.5232]
	1	0.9299	3.3651	5.8647	[−4.2286, 3.5829]
	2	0.9304	3.5570	5.6733	[−3.9198, 3.6944]
	3	0.9499	3.2267	5.1857	[−2.1618, 3.3769]
	4	0.9722	2.5953	3.2854	[−2.1597, 2.0604]
$PCF_B^U(m)$ ($1 \leq m \leq 10$)	5	0.9739	2.7549	3.4112	[−2.2424, 1.5691]
	6	0.9811	2.6248	3.2604	[−1.6623, 2.0491]
	7	0.9811	3.0305	3.2627	[−1.6872, 2.0506]
	1	0.9374	4.5860	8.4552	[−4.7129, 2.3390]
	2	0.9866	2.2673	4.3561	[−2.0249, 0.9044]
	3	0.9915	1.9535	3.8875	[−1.8070, 0.7175]
	4	0.9938	1.8246	3.0459	[−1.4158, 0.7629]
	5	0.9938	2.0375	3.0883	[−1.4355, 0.7282]
	6	0.9950	2.1070	2.5237	[−1.1731, 0.7826]
	7	0.9969	2.0443	1.7935	[−0.8337, 0.7835]

non-dominated optimal solutions. The engineers can make their own decision according to the actual demand from the obtained Pareto front [48].

5.2. MOD of FLGFTs of type A

According to the methodology mentioned in Section 5.1, the accuracies of different polynomial functions for the type A-FLGFTs and the corresponding UFTs with orders ranging from 1 to 7 are summarized in Table 4. From Table 4, it can be found that the 7th-order polynomial functions are the most accurate ones in most cases, respectively. Although the most accurate metamodels are the 6th-order polynomial functions in three cases among the total 16 cases, the deviations between these 6th-order polynomial functions and the corresponding 7th-order polynomial functions are very small in the three cases. The deviations can be ignored in these cases. Apparently, it can be found that the 7th-order polynomial functions of SEA and PCF are accurate enough for the optimization design in engineering. Thus, for unity a 7th-order polynomial function is selected in the following optimization de-

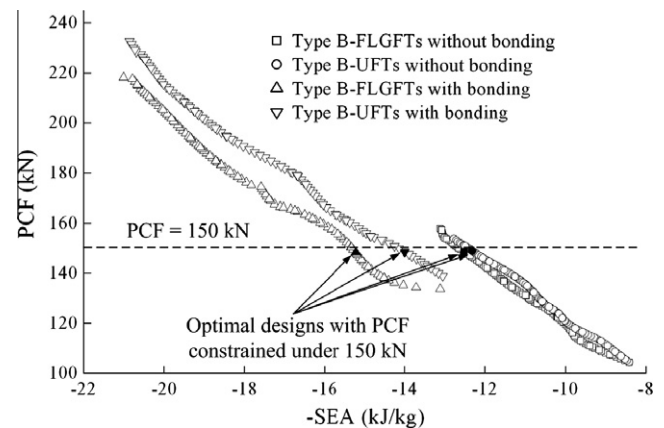


Fig. 15. Pareto fronts of the type B-FLGFTs and the corresponding UFTs.

sign. The metamodels of type A-FLGFTs without bonding are established as follows:

$$SEA_{NB}^G(m) = \begin{cases} 8.46378005 + 33.28456843m - 266.91393267m^2 \\ + 1144.15889430m^3 - 2633.88368940m^4 \\ + 3313.13819814m^5 - 2143.76368761m^6 \\ + 557.31787008m^7 \quad (0 \leq m \leq 1) \\ 8.35048000 + 5.68421113m - 2.98553132m^2 \\ + 0.89413088m^3 - 0.15855558m^4 + 0.01645394m^5 \\ - 0.00092285m^6 + 2.15937216 \times 10^{-5}m^7 \\ (1 < m \leq 10) \end{cases} \quad (21)$$

$$SEA_B^G(m) = \begin{cases} 12.83554175 + 92.17202304m - 676.97641712m^2 \\ + 2616.53878033m^3 - 5585.97991991m^4 \\ + 6661.85035753m^5 - 4157.36807537m^6 \\ + 1057.18359673m^7 \quad (0 \leq m \leq 1) \\ 14.90243995 + 9.27446797m - 5.34086785m^2 \\ + 1.70021023m^3 - 0.31527264m^4 + 0.03386223m^5 \\ - 0.00195092m^6 + 4.66024770 \times 10^{-5}m^7 \\ (1 < m \leq 10) \end{cases} \quad (25)$$

$$PCF_{NB}^G(m) = \begin{cases} 104.44308166 + 285.70056259m - 1972.95735526m^2 \\ + 7679.14413166m^3 - 16367.50726891m^4 \\ + 19309.11606979m^5 - 11825.86489105m^6 \\ + 2929.09632206m^7 \quad (0 \leq m \leq 1) \\ 90.77679892 + 89.76615119m - 55.35575941m^2 \\ + 19.50325932m^3 - 3.95019336m^4 + 0.45508450m^5 \\ - 0.02770085m^6 + 0.00069108m^7 \\ (1 < m \leq 10) \end{cases} \quad (22)$$

$$PCF_B^G(m) = \begin{cases} 136.63294138 + 356.00275365m - 911.98960161m^2 \\ + 665.08314419m^3 + 1205.78076935m^4 \\ - 2274.53805923m^5 + 1158.70073318m^6 \\ - 124.88321400m^7 \quad (0 \leq m \leq 1) \\ 19.45179696 + 363.13691008m - 240.89306608m^2 \\ + 83.91720274m^3 - 16.57445099m^4 + 1.86706071m^5 \\ - 0.11170309m^6 + 0.00275155m^7 \\ (1 < m \leq 10) \end{cases} \quad (26)$$

Metamodels of corresponding UFTs of type A-FLGFTs without bonding are as follows:

$$SEA_{NB}^U(m) = \begin{cases} 8.39121853 + 22.10343933m - 125.61082278m^2 \\ + 382.24378216m^3 - 594.73014307m^4 \\ + 446.11843991m^5 - 118.33004904m^6 \\ - 8.74183458m^7 \quad (0 \leq m \leq 1) \\ 8.17511999 + 5.33810931m - 2.78234549m^2 \\ + 0.85577948m^3 - 0.15819386m^4 + 0.01718382m^5 \\ - 0.00100726m^6 + 2.45232271 \times 10^{-5}m^7 \\ (1 < m \leq 10) \end{cases} \quad (23)$$

Metamodels of corresponding UFTs of type A-FLGFTs with bonding are as follows:

$$SEA_B^U(m) = \begin{cases} 12.83344130 + 41.70477617m - 310.63506085m^2 \\ + 1271.80986476m^3 - 2811.46230006m^4 \\ + 3426.06548500m^5 - 2167.71630001m^6 \\ + 555.92898035m^7 \quad (0 \leq m \leq 1) \\ 16.09310011 + 2.41586632m + 0.41865218m^2 \\ - 0.54174503m^3 + 0.15986994m^4 - 0.02243249m^5 \\ + 0.00154702m^6 - 4.20868389 \times 10^{-5}m^7 \\ (1 < m \leq 10) \end{cases} \quad (27)$$

$$PCF_{NB}^U(m) = \begin{cases} 103.98292823 + 234.55129275m - 1618.48151994m^2 \\ + 6572.90365314m^3 - 14583.01929855m^4 \\ + 17835.30489349m^5 - 11297.94829559m^6 \\ + 2892.85684061m^7 \quad (0 \leq m \leq 1) \\ 79.053199738 + 120.22177118m - 86.05932251m^2 \\ + 33.26248632m^3 - 7.15292099m^4 + 0.85769662m^5 \\ - 0.05361895m^6 + 0.00136098m^7 \\ (1 < m \leq 10) \end{cases} \quad (24)$$

$$PCF_B^U(m) = \begin{cases} 136.76855020 + 580.93761580m - 4970.39128327m^2 \\ + 19929.55937672m^3 - 40538.19807434m^4 \\ + 44022.43115616m^5 - 24398.21646881m^6 \\ + 5432.53898144m^7 \quad (0 \leq m \leq 1) \\ 232.80820945 - 135.41016823m + 153.98312026m^2 \\ - 71.00984874m^3 + 16.94305971m^4 - 2.18657347m^5 \\ + 0.14450425m^6 - 0.00382919m^7 \\ (1 < m \leq 10) \end{cases} \quad (28)$$

Metamodels of type A-FLGFTs with bonding are obtained as:

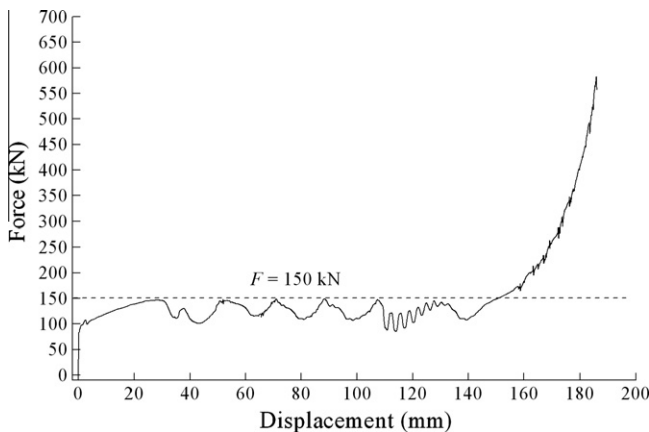


Fig. 16. Axial force–displacement curve of the overall optimal design with PCF constrained under 150 kN.

Based on the metamodels, the Pareto fronts of type A-FLGFTs and the corresponding UFTs without bonding and with bonding for the optimization problem defined as Eq. (14) are obtained and shown in Fig. 13 by using the MOPSO algorithm. It can be easily found that the Pareto fronts of type A-FLGFTs without bonding and with bonding are more predominant than that of the corresponding UFTs, respectively. In other words, the energy absorption capacity per unit mass of type A-FLGFTs without bonding (or with bonding) is better than that of the corresponding UFTs when PCF is constrained under the same level. In addition, it can be seen from Fig. 13 that the Pareto fronts of type A-FLGFTs with bonding are located on the left hand side of the Pareto front of type A-FLGFTs without bonding. This indicate that the energy absorption capacity per unit mass of the type A-FLGFTs with bonding is better than that of the type A-FLGFTs without bonding when PCF is constrained under the same level. When the PCF of a structure is needed to be constrained under the level of 150 kN in engineering, the optimal designs of the type A-FLGFTs without bonding and with bonding correspond to the Pareto points which are marked as solid square and triangle (up) in Fig. 13, respec-

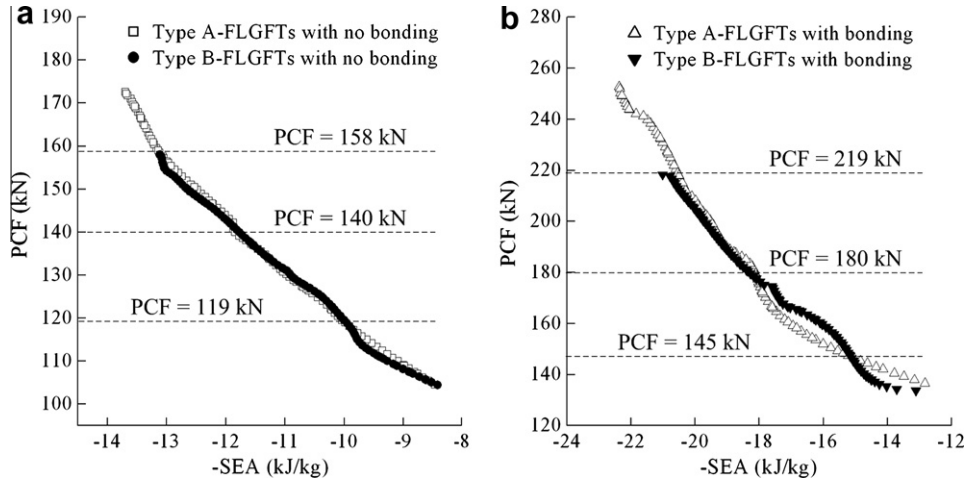


Fig. 17. Comparison of Pareto fronts of the type A-FLGFTs and the type B-FLGFTs: (a) without bonding and (b) with bonding.

tively. And, the optimal designs (PCF constrained under 150 kN) of the type A-FLGFTs without bonding and with bonding correspond to the Pareto points marked as solid circle and triangle (down) in Fig. 13, respectively. The detailed design parameters of these optimal designs are listed in Table 5. Then, the finite element models for the optimal designs are established. The comparison between the FEA results and the approximate results are shown in Table 5. It can be found that the absolute errors are less 5%, which is acceptable in engineering design. The deformation profiles of these optimal designs compressed by 120 mm are shown in Fig. 14a–d. The collapse modes of the bonded cases are distinctly different from that of the non-bonded ones. The extensional folding mode occurs in the bonded cases, while the mixed folding mode appears in the non-bonded cases. The folds of the tubes do not obviously encroach into the filled foams in the non-bonded cases. On the contrary, the tubes tightly cling to the filled foams and fold together with the foams in the bonded cases. This leads to additional compression for the foams and make it harder to collapse for the tubes. This is the reason why the type A-FLGFTs with bonding can absorb more energy than the type A-FLGFTs without bonding.

5.3. MOD of FLGFTs of type B

For type B-FLGFTs and the corresponding UFTs, the polynomial functions of SEA and PCF are constructed and the accuracies of these different polynomial functions with orders ranging from 1 to 7 are listed in Table 6. The 7th-order polynomial function is the most accurate one in each case except for only one case. In this case, the most accurate metamodel is the 6th-order polynomial function. But, the little deviation between 6th-order polynomial function and the corresponding 7th-order polynomial function can be ignored. Thus, for unity a 7th-order polynomial function is selected as the metamodel of the type B-FLGFTs and the corresponding UFTs in the following optimization design. The metamodels of type B-FLGFTs without bonding are given as:

$$SEA_{NB}^G(m) = \begin{cases} 8.41989558 + 26.00835912m - 203.83874517m^2 \\ + 837.41566229m^3 - 1882.97737360m^4 \\ + 2353.11459088m^5 - 1529.08727598m^6 \\ + 401.98992252m^7 \quad (0 \leq m \leq 1) \\ 9.35774000 + 2.40863742m - 0.92241834m^2 \\ + 0.23369758m^3 - 0.03814163m^4 + 0.00382231m^5 \\ - 0.00021231m^6 + 4.97082215 \times 10^{-6}m^7 \\ (1 < m \leq 10) \end{cases} \quad (29)$$

$$PCF_{NB}^G(m) = \begin{cases} 104.43605657 + 161.10946038m - 1076.28278744m^2 \\ + 4268.41204357m^3 - 9300.54693222m^4 \\ + 11247.53175735m^5 - 7085.66928673m^6 \\ + 1812.61652994m^7 \quad (0 \leq m \leq 1) \\ 127.33660209 - 8.06119436m + 20.86255306m^2 \\ - 10.95185292m^3 + 2.77579396m^4 - 0.37498573m^5 \\ + 0.02587801m^6 - 0.00071605m^7 \\ (1 < m \leq 10) \end{cases} \quad (30)$$

Metamodels of corresponding UFTs of type B-FLGFTs without bonding are as follows:

$$SEA_{NB}^U(m) = \begin{cases} 8.41694786 + 10.92859036m - 80.77984635m^2 \\ + 403.85365164m^3 - 1054.85214472m^4 \\ + 1447.55338216m^5 - 994.30137706m^6 \\ + 269.82957232m^7 \quad (0 \leq m \leq 1) \\ 10.41929997 \\ - 0.31041173m + 0.78332619m^2 - 0.28831901m^3 \\ + 0.04894242m^4 - 0.00418550m^5 + 0.00016397m^6 \\ - 1.93977488 \times 10^{-6}m^7 \quad (1 < m \leq 10) \end{cases} \quad (31)$$

$$PCF_{NB}^U(m) = \begin{cases} 104.43449198 + 126.63247889m - 786.20898604m^2 \\ + 3089.21287918m^3 - 6719.13414192m^4 \\ + 8123.26727295m^5 - 5118.13676834m^6 \\ + 1309.64038515m^7 \quad (0 \leq m \leq 1) \\ 110.80700000 + 26.55281603m - 9.59078309m^2 \\ + 2.23592678m^3 - 0.32857157m^4 + 0.02923734m^5 \\ - 0.00143541m^6 + 2.98085961 \times 10^{-5}m^7 \\ (1 < m \leq 10) \end{cases} \quad (32)$$

Metamodels of type B-FLGFTs with bonding are obtained as:

$$SEA_B^G(m) = \begin{cases} 12.97333100 + 31.61973954m - 202.81077445m^2 \\ + 766.10678732m^3 - 1582.71906638m^4 \\ + 1802.78212595m^5 - 1066.12489653m^6 \\ + 256.01070839m^7 \quad (0 \leq m \leq 1) \\ 15.28804001 + 3.17505353m - 0.60646951m^2 \\ - 0.05470927m^3 + 0.04266235m^4 - 0.00721747m^5 \\ + 0.00053878m^6 - 1.54505154 \times 10^{-5}m^7 \\ (1 < m \leq 10) \end{cases} \quad (33)$$

$$PCF_B^C(m) = \begin{cases} 133.82643417 - 11.49775293m + 1293.41023731m^2 \\ -6941.32200527m^3 + 18283.33743095m^4 \\ -26313.49842834m^5 + 19549.53258896m^6 \\ -5818.56860542m^7 \quad (0 \leq m \leq 1) \\ 166.28319989 - 7.86985162m + 26.74142438m^2 \\ -12.32818969m^3 + 2.62825964m^4 - 0.29065900m^5 \\ +0.01599939m^6 - 0.00034279m^7 \\ (1 < m \leq 10) \end{cases} \quad (34)$$

Metamodels of corresponding UFTs of type B-FLGFTs with bonding are as follows:

$$SEA_B^U(m) = \begin{cases} 13.05203268 + 23.98268096m - 130.11994371m^2 \\ +341.94524658m^3 - 382.46449280m^4 \\ +63.71815491m^5 + 188.10783029m^6 \\ -101.48809147m^7 \quad (0 \leq m \leq 1) \\ 10.94545977 + 10.58798629m - 6.90561186m^2 \\ +2.60848641m^3 - 0.56612383m^4 + 0.06946883m^5 \\ -0.00446564m^6 + 0.00011661m^7 \\ (1 < m \leq 10) \end{cases} \quad (35)$$

$$PCF_B^U(m) = \begin{cases} 138.83969848 + 264.89687084m - 1767.59453428m^2 \\ +5805.67625713m^3 - 9399.46383667m^4 \\ +7111.77243423m^5 - 1648.74154663m^6 \\ -325.86375713m^7 \quad (0 \leq m \leq 1) \\ 114.83339410 + 129.47846287m - 97.24013698m^2 \\ +40.68926151m^3 - 9.48399021m^4 + 1.22726135m^5 \\ -0.08222606m^6 + 0.00221977m^7 \\ (1 < m \leq 10) \end{cases} \quad (36)$$

By using the metamodels and the MOPSO algorithm, the Pareto fronts of type B-FLGFTs and the corresponding UFTs without bonding and with bonding for the optimization problem defined as Eq. (14) are obtained and shown in Fig. 15. It can be easily found from Fig. 15 that the Pareto fronts of type B-FLGFTs without bonding and with bonding are more predominant than that of the corresponding UFTs, respectively. This means that the energy absorption capacity per unit mass of type B-FLGFTs without bonding (or with bonding) is better than that of the corresponding UFTs with PCF constrained under the same level. This observation is the same as that of type A-FLGFTs. Moreover, it can be seen from Fig. 15 that the Pareto fronts of type B-FLGFTs with bonding are located on the left hand side of the Pareto front of type B-FLGFTs without bonding. This indicates that the energy absorption capacity per unit mass of the type B-FLGFTs with bonding is better than that of the type B-FLGFTs without bonding when PCF is constrained under the same level. This is also the same as that of the type A-FLGFTs. The optimal designs of the type B-FLGFTs without bonding and with bonding with PCF constrained under 150 kN correspond to the solid square and triangle (up) points in Fig. 15, respectively. The Pareto points marked as solid circle and triangle (down) in Fig. 15 represent the optimal designs (PCF constrained under 150 kN) of the corresponding UFTs without bonding and with bonding, respectively. Their detailed design parameters and their FEA results are summarized in Table 5. The absolute errors between FEA results and the metamodels are less than 1%, which indicate that the 7th-order polynomial functions for the type B cases are very accurate. The deformation profiles of these optimal designs compressed by 120 mm are shown in Fig. 14e–h. The same phenomenon as the type A cases can be easily found. For the type B

Table 7

The relationship between the crashworthiness of the type A-FLGFTs and that of the type B-FLGFTs.

Relationship of crashworthiness	Constraint of PCF (kN)
<i>Without bonding</i>	
Type B-FLGFT \geq Type A-FLGFT	PCF \leq 140–158
Type A-FLGFT \geq Type B-FLGFT	PCF \leq 119–140
Type B-FLGFT \geq Type A-FLGFT	PCF \leq 119
<i>With bonding</i>	
Type B-FLGFT \geq Type A-FLGFT	PCF \leq 180–219
Type A-FLGFT \geq Type B-FLGFT	PCF \leq 145–180
Type B-FLGFT \geq Type A-FLGFT	PCF \leq 145

cases, the collapse modes of the bonded cases are extremely different from that of the non-bonded ones. The extensional folding mode and the mixed folding mode occur in the bonded and non-bonded cases, respectively. In the non-bonded cases, the folds of the tubes do not clearly encroach into the filled foams. In contrast, the tubes tightly cling to the filled foams and fold together with the foams in the bonded cases. Just because of this, the bonded cases can absorb more impact energy than the non-bonded cases for the cases of type B.

Overall, the optimal design with PCF constrained under 150 kN is the bonded type A-FLGFT with $m = 0.0384$. The force–displacement curve of this optimal design obtained by FEA is plotted in Fig. 16. It can be found that the PCF when the type A-FLGFT with bonding is compressed by 120 mm is exactly near to but still less than 150 kN.

The comparison of Pareto fronts of the type A-FLGFTs and the type B-FLGFTs without bonding and with bonding are shown in Fig. 17a and b, respectively. From Fig. 17a and b, it can be found that the range of the optimal solutions of the type A-FLGFTs without bonding and with bonding are relatively wider than that of the type B-FLGFTs, respectively. In addition, it can be found that the Pareto fronts of the type A-FLGFTs (or type B-FLGFTs) without bonding and with bonding do not always perform more predominantly than that of the type B-FLGFTs (or type A-FLGFTs), respectively. This is to say that the energy absorption capacity of the type A-FLGFTs (or type B-FLGFTs) without bonding and with bonding is not absolutely better than that of the type B-FLGFTs (or type A-FLGFTs), respectively. Based on Fig. 17, the detailed relationship between the crashworthiness of the type A-FLGFTs and that of the type B-FLGFTs is shown in Table 7.

6. Conclusions

In this paper, two kinds of functionally lateral graded foam-filled tubes (type A-FLGFTs and type B-FLGFTs) without bonding and with bonding subjected to axial dynamic loading have been investigated by employing finite element code LS-DYNA. A series of lateral graded and uniform foam-filled tubes with the same weight are compared for their energy absorption characteristics. The numerical results show that the crashworthiness of both of type A-FLGFTs and type B-FLGFTs are better than that of the corresponding uniform foam-filled tubes (UFTs). In addition, it can also be found that the adhesive bond between the filled foam and the tube can largely improve the crashworthiness of the FLGFTs.

In order to seek the optimal designs of type A-FLGFTs and type B-FLGFTs, multiobjective optimization using the multiobjective particle swarm optimization (MOPSO) algorithm has been presented. The 7th-order polynomial functions of the objectives on SEA and peak crushing force (PCF) are established and are found to be accurate enough for optimization design in engineering. The obtained Pareto fronts of the two kinds of FLGFTs and the corresponding UFTs indicate that the FLGFTs are generally superior to

the corresponding UFTs for both of the non-bonded and bonded cases.

Acknowledgments

This work was supported by the Young Teacher Development Plan of Hunan University and the Cultivation Fund of the Key Scientific and National Science and Technology Support Program (No. 2012BAH09B02) and Technical Innovation Project, Ministry of Education of China (No. 11072074) and the Open Fund of the State Key Laboratory of Advanced Design and Manufacturing for Vehicle Body of Hunan University (Nos. 30815007 and 30915001).

References

- [1] Ahmad Z, Thambiratnam DP. Application of foam-filled conical tubes in enhancing the crashworthiness performance of vehicle protective structures. *Int J Crashworthines* 2009;14(4):349–63.
- [2] Seitzberger M, Rammerstorfer FG, Degiseher HP, Grading R. Crushing of axially compressed steel tubes filled with aluminium foam. *Acta Mech* 1997;125(1–4):93–105.
- [3] Reid SR, Reddy TY, Gray MD. Static and dynamic axial crushing of foam-filled sheet metal tubes. *Int J Mech Sci* 1986;28(5):295–322.
- [4] Reid SR, Reddy TY. Axial crushing of foam-filled tapered sheet metal tubes. *Int J Mech Sci* 1986;28(10):643–56.
- [5] Reddy TY, Wall RJ. Axial compression of foam-filled thin-walled circular tubes. *Int J Impact Eng* 1988;7(2):151–66.
- [6] Santosa SP, Wierzbicki T, Hanssen AG, Langseth Magnus. Experimental and numerical studies of foam-filled sections. *Int J Impact Eng* 2000;24(5):509–34.
- [7] Hanssen AG, Langseth M, Hopperstad OS. Static and dynamic crushing of circular aluminium extrusions with aluminium foam filler. *Int J Impact Eng* 2000;24(5):475–507.
- [8] Hanssen AG, Langseth M, Hopperstad OS. Static and dynamic crushing of square aluminium extrusions with aluminium foam filler. *Int J Impact Eng* 2000;24(4):347–83.
- [9] Seitzberger M, Rammerstorfer FG, Grading R, Degischer HP, Blaimschein M, Walch C. Experimental studies on the quasi-static axial crushing of steel columns filled with aluminium foam. *Int J Solids Struct* 2000;37(30):4125–47.
- [10] Kavi H, Toksoy AK, Guden M. Predicting energy absorption in a foam-filled thin-walled aluminum tube based on experimentally determined strengthening coefficient. *Mater Des* 2006;27(4):263–9.
- [11] Abramowicz W, Wierzbicki T. Axial crushing of foam-filled columns. *Int J Mech Sci* 1988;30(3/4):263–71.
- [12] Wang QC, Fan ZJ, Gui LJ. Theoretical analysis for axial crushing behaviour of aluminium foam-filled hat sections. *Int J Mech Sci* 2007;49(4):515–21.
- [13] Wang QC, Fan ZJ, Gui LJ. A theoretical analysis for the dynamic axial crushing behaviour of aluminium foam-filled hat sections. *Int J Solids Struct* 2006;43(7–8):2064–75.
- [14] Mahmoudabadi MZ, Sadighi M. A study on the static and dynamic loading of the foam filled metal hexagonal honeycomb – Theoretical and experimental. *Mater Sci Eng A* 2011;530:333–43.
- [15] Ahmad Z, Thambiratnam DP. Crushing response of foam-filled conical tubes under quasi-static axial loading. *Mater Des* 2009;30(7):2393–403.
- [16] Aktay L, Kröplin BH, Toksoy AK, Guden M. Finite element and coupled finite element/smooth particle hydrodynamics modeling of the quasi-static crushing of empty and foam-filled single, bitubular and constraint hexagonal- and square-packed aluminum tubes. *Mater Des* 2008;29(5):952–62.
- [17] Mirfendereski L, Salimi M, Ziaei-Rad S. Parametric study and numerical analysis of empty and foam-filled thin-walled tubes under static and dynamic loadings. *Int J Mech Sci* 2008;50(6):1042–57.
- [18] Meguid SA, Attia MS, Monfort A. On the crush behaviour of ultralight foam-filled structures. *Mater Des* 2004;25(3):183–9.
- [19] Shahbeyk S, Petrinic N, Vafai A. Numerical modelling of dynamically loaded metal foam-filled square columns. *Int J Impact Eng* 2007;34(3):573–86.
- [20] Zarei HR, Kröger M. Optimization of the foam-filled aluminum tubes for crush box application. *Thin Wall Struct* 2008;46(2):214–21.
- [21] Zarei HR, Kröger M. Crashworthiness optimization of empty and filled aluminum crash boxes. *Int J Crashworthines* 2007;12(3):255–64.
- [22] Hou SJ, Li Q, Long SY, Yang XJ, Li W. Crashworthiness design for foam filled thin-wall structures. *Mater Des* 2009;30(6):2024–32.
- [23] Hou SJ, Han X, Sun GY, Long SY, Yang XJ, Li W, et al. Multiobjective optimization for tapered circular tubes. *Thin Wall Struct* 2011;49(7):855–63.
- [24] Bi J, Fang HB, Wang Q, Ren XC. Modeling and optimization of foam-filled thin-walled columns for crashworthiness designs. *Finite Elem Anal Des* 2010;46(9):698–709.
- [25] Zhang Y, Sun GY, Li GY, Luo Z, Li Q. Optimization of foam-filled bitubular structures for crashworthiness criteria. *Mater Des* 2012;38:99–109.
- [26] Cui L, Kiernan S, Gilchrist MD. Designing the energy absorption capacity of functionally graded foam materials. *Mater Sci Eng A – Struct* 2009;507(1–2):215–25.
- [27] Kiernan S, Cui L, Gilchrist MD. A numerical investigation of the dynamic behaviour of functionally graded foams. *Int J Nonlinear Mech* 2009;44(5):456–68.
- [28] Gupta N, Ricci W. Comparison of compressive properties of layered syntactic foams having gradient in microballoon volume fraction and wall thickness. *Mater Sci Eng A* 2006;427(1–2):331–42.
- [29] Gupta N. A functionally graded syntactic foam material for high energy absorption under compression. *Mater Lett* 2007;61(4–5):979–82.
- [30] Sun GY, Li GY, Hou SJ, Zhou SW, Li W, Li Q. Crashworthiness design for functionally graded foam-filled thin-walled structures. *Mater Sci Eng A* 2010;527(7–8):1911–9.
- [31] Nouraei H. Nonlinear FEA of the crush behaviour of functionally graded foam-filled columns. A thesis submitted in conformity with the requirements for the degree of master of applied science, Department of mechanical and industrial engineering, University of Toronto, 2010.
- [32] Kim HS. New extruded multi-cell aluminum profile for maximum crash energy absorption and weight efficiency. *Thin Wall Struct* 2002;40(4):311–27.
- [33] Zhang ZH, Liu ST, Tang ZL. Crashworthiness investigation of kagome honeycomb sandwich cylindrical column under axial crushing loads. *Thin Wall Struct* 2010;48(1):9–18.
- [34] Hallquist JO. LS-DYNA theoretical manual. California: Livemore Software Technology Corporation; 1998.
- [35] Hallquist JO. LS-DYNA keyword user's manual. California: Livemore Software Technology Corporation; 2003.
- [36] Santosa S, Wierzbicki T. Crash behavior of box columns filled with aluminium honeycomb or foam. *Comput Struct* 1998;68(4):343–67.
- [37] Zhang ZH, Liu ST, Tang ZL. Comparisons of honeycomb sandwich and foam-filled cylindrical columns. *Thin Wall Struct* 2011;49(9):1071–9.
- [38] Deshpande VS, Fleck NA. Isotropic constitutive models for metallic foams. *J Mech Phys Solids* 2000;48(6–7):1253–83.
- [39] Hanssen AG, Hopperstad OS, Langseth M, Ilstad H. Validation of constitutive models applicable to aluminium foams. *Int J Mech Sci* 2002;44(2):359–406.
- [40] Reyes A, Hopperstad OS, Berstad T, Hanssen AG, Langseth M. Constitutive modeling of aluminum foam including fracture and statistical variation of density. *Eur J Mech A – Solid* 2003;22(6):815–35.
- [41] Abramowicz W, Jones N. Dynamic progressive buckling of circular and square tubes. *Int J Impact Eng* 1986;4(4):243–70.
- [42] Yin HF, Wen GL, Hou SJ, Chen K. Crushing analysis and multiobjective crashworthiness optimization of honeycomb-filled single and bitubular polygonal tubes. *Mater Des* 2011;32(8):4449–60.
- [43] Wang GG, Shan S. Review of metamodeling techniques in support of engineering design optimization. *ASME Trans J Mech Des* 2007;129(4):370–80.
- [44] Kleijnen JPC. An overview of the design and analysis of simulation experiments for sensitivity analysis. *Eur J Oper Res* 2005;164(2):287–300.
- [45] Hou SJ, Li Q, Long SY, Yang XJ, Li W. Multiobjective optimization of multi-cell sections for the crashworthiness design. *Int J Impact Eng* 2008;35(11):1167–355.
- [46] Kurtaran H, Eskandarian A, Marzougou D. Crashworthiness design optimization using successive response surface approximations. *Comput Mech* 2002;29(4–5):409–21.
- [47] Forsberg J, Nilsson L. Evaluation of response surface methodologies used in crashworthiness optimization. *Int J Impact Eng* 2006;32(5):759–77.
- [48] Liao XT, Li Q, Yang XJ, Zhang WG, Li W. Multiobjective optimization for crash safety design of vehicles using stepwise regression model. *Struct Multidiscip Optim* 2008;35(6):561–9.
- [49] Raquel C, Naval P. An effective use of crowding distance in multiobjective particle swarm optimization. In: Proceedings of the 2005 conference on genetic and evolutionary computation, Washington (DC), USA; 2005. p. 257–64.
- [50] Liu DS, Tan KC, Goh CK, Ho WK. A multiobjective memetic algorithm based on particle swarm optimization. *IEEE Trans Syst Man Cybernet B* 2007;37(1):42–50.